Submission to ***Molecular Imaging and Biology***
Manuscript category: Research Article
Manuscript No.: MIBI-D-24-00060.R2, 2nd revision

# Partial acquisition of spectral projections accelerates four-dimensional spectral-spatial EPR imaging for mouse tumor models: A feasibility study

Misa Oba,[1] Mai Taguchi,[1] Yohei Kudo,[1] Koya Yamashita,[2] Hironobu Yasui,[3] Shingo Matsumoto,[4] Igor A. Kirilyuk,[5] Osamu Inanami,[3] Hiroshi Hirata[4*]

[1] Division of Bioengineering and Bioinformatics, Graduate School of Information Science and Technology, Hokkaido University, North 14, West 9, Kita-ku, Sapporo, 060-0814, Japan

[2] Laboratory of Radiation Biology, Graduate School of Veterinary Medicine, Hokkaido University, North 18, West 9, Kita-ku, Sapporo, 060-0818, Japan

[3] Laboratory of Radiation Biology, Faculty of Veterinary Medicine, Hokkaido University, North 18, West 9, Kita-ku, Sapporo, 060-0818, Japan

[4] Division of Bioengineering and Bioinformatics, Faculty of Information Science and Technology, Hokkaido University, North 14, West 9, Kita-ku, Sapporo, 060-0814, Japan

[5] N. N. Vorozhtsov Novosibirsk Institute of Organic Chemistry, 9, Ac. Lavrentieva Ave., Novosibirsk, 630090, Russia

* Corresponding author
Hiroshi Hirata, Ph.D.
Phone: +81-11-706-6762
E-mail: hhirata@ist.hokudai.ac.jp

Short running title: Partial acquisition of 4D spectral-spatial EPR imaging

Word counts: 7,678 words (abstract, main text, figure legends, and references)
Number of Figures: 5

**Abstract**

*Purpose:* Our study aimed to accelerate the acquisition of four-dimensional (4D) spectral-spatial electron paramagnetic resonance (EPR) imaging for mouse tumor models. This advancement in EPR imaging should reduce the acquisition time of spectroscopic mapping while reducing quality degradation for mouse tumor models.

*Procedures:* EPR spectra under magnetic field gradients, called spectral projections, were partially measured. Additional spectral projections were later computationally synthesized from the measured spectral projections. Four-dimensional spectral-spatial images were reconstructed from the post-processed spectral projections using the algebraic reconstruction technique (ART) and assessed in terms of their image qualities. We applied this approach to a sample solution and a mouse Hs766T xenograft model of human-derived pancreatic ductal adenocarcinoma cells to demonstrate the feasibility of our concept. The nitroxyl radical imaging agent $^{2}$H,$^{15}$N-DCP was exogenously infused into the mouse xenograft model.

*Results:* The computation code of 4D spectral-spatial imaging was tested with numerically generated spectral projections. In the linewidth mapping of the sample solution, we achieved a relative standard uncertainty (standard deviation/| mean |) of 0.76 μT/45.38 μT = 0.017 on the peak-to-peak first-derivative EPR linewidth. The qualities of the linewidth maps and the effect of computational synthesis of spectral projections were examined. Finally, we obtained the three-dimensional linewidth map of $^{2}$H,$^{15}$N-DCP in a Hs766T tumor-bearing leg *in vivo*.

*Conclusion:* We achieved a 46.7% reduction in the acquisition time of 4D spectral-spatial EPR imaging without significantly degrading the image quality. A combination of ART and partial acquisition in three-dimensional raster magnetic field gradient settings in orthogonal coordinates is a novel approach. Our approach to 4D spectral-spatial EPR imaging can be applied to any subject, especially for samples with less variation in one direction.

**Keywords:**

EPR; EPR imaging; 4D spectral-spatial imaging; accelerated image acquisition; mouse xenograft model; linewidth mapping.

## Introduction

A lack of adequate oxygen supply (hypoxia) and acidification in the extracellular space (acidosis) are the hallmarks of solid tumors and indicate tumor metabolic shifts and malignancy, such as the migration, invasion, and metastasis of cancer cells [1, 2]. Furthermore, hypoxia in solid tumors is associated with resistance to chemotherapy and radiation therapy [3]. Therefore, tumor tissue oxygenation is essential to understand the pathophysiological state of tumors [4]. Noninvasive measurements of the partial pressure of oxygen ($pO_2$) in tumor tissue provide insight into a critical parameter in the microenvironment of cancer cells [5]. Several imaging modalities can be used to visualize oxygen-related parameters in tumors, such as blood oxygen saturation with photoacoustic imaging [6], hypoxic cells with positron emission tomography (PET) using the hypoxia radiotracer $^{18}$F-misonidazole ($^{18}$F-MISO) [7], and the change in the magnetic properties of oxygenated and deoxygenated hemoglobin with blood oxygen level-dependent magnetic resonance imaging (BOLD MRI) [8]. However, these imaging modalities do not provide $pO_2$ directly. The quantitative measurement of $pO_2$ is preferable for monitoring tumor tissue oxygenation, which is related to the radiation sensitivity of cancer cells and the effects of anticancer drugs.

Electron paramagnetic resonance (EPR) can be used to measure $pO_2$ in biological tissues *in vivo* [9, 10]. $pO_2$ can be estimated using the shift in the absorption linewidth of unpaired electrons (with continuous-wave (CW) EPR) or the shift in the relaxation time of unpaired electrons (with pulsed EPR) [11]. In the CW-EPR protocol, mapping a spectroscopic parameter, e.g., the absorption linewidth, which is sensitive to $pO_2$ or the ratio of two absorption peaks that are sensitive to pH, requires spectral-spatial data (each pixel or voxel has EPR spectral data) [12]. Such an imaging approach requires thousands of EPR spectra under magnetic field gradients, called spectral projections, to reconstruct the spectral

lineshape at each voxel in three-dimensional (3D) space. This spectroscopic mapping is called four-dimensional (4D) spectral-spatial imaging [13–15]. While pulsed EPR has been successfully applied to tumor $pO_2$ mapping using an oxygen-sensitive imaging agent such as the triarylmethyl radical OX063, it is still difficult to use pulsed EPR to detect an imaging agent with a shorter relaxation time or a broader absorption peak. Therefore, versatile CW-EPR detection is preferable for these imaging agents, e.g., oxygen- or pH-sensitive nitroxyl radical agents [16, 17]. However, a longer acquisition time of 4D spectral-spatial EPR imaging is a drawback in small animal experiments.

There are two approaches to reducing the acquisition time of 4D spectral-spatial EPR imaging with the CW protocol. One is fast magnetic field scanning to record each EPR spectrum in a short duration [18, 19]. Rapid-scan EPR is another approach to reducing the time needed to record each EPR spectrum [20]. The other approach is to acquire fewer spectral projections [21, 22]. While compressed sensing is a powerful method for reconstructing a spatial image from sparsely sampled data in MRI and EPR imaging [23–26], compressed sensing for 4D spectral-spatial EPR imaging has not yet been reported. Recently, a convex, constrained optimization-based 4D spectral-spatial EPR imaging with limited angular ranges or sparse sampling has been reported [27, 28]. Magnetic field gradient (MFG) settings with half-sphere acquisition in polar coordinates are commonly used for projection-based 4D spectral-spatial imaging [8, 12–14, 29–31]. Also, 3D raster MFG settings in orthogonal coordinates have been used for 4D spectral-spatial imaging with the algebraic reconstruction technique (ART) [15, 32–34] [see Suppl. Table S1 in the Electronic Supplementary Material (ESM)]. We must further explore emerging methods to reduce the acquisition time and suitable image reconstruction techniques that fit our EPR imaging setup. Therefore, an approach to reducing the number of measured spectral projections has been needed in CW-EPR-based spectral-spatial imaging. Faced with this technical challenge, we

must fill the gap between the current acquisition approach and the promising accelerated acquisition approach with minimal degradation of the image quality.

This study aimed to reduce the number of measured spectral projections with minimal degradation of the resultant image quality in 4D spectral-spatial imaging. We demonstrate that the partial acquisition strategy for spectral projections accelerates 4D spectral-spatial EPR imaging, i.e., mapping the EPR absorption linewidth. To this end, we introduced a computational synthesis of EPR spectra from measured spectra in addition to the partial acquisition approach for 3D raster MFG settings in orthogonal coordinates in ART, which is a novel combination. This article describes the effectiveness of partially acquiring spectral projections and the computational synthesis of additional EPR spectra with an assessment of image quality for a sample solution and a mouse tumor model *in vivo*.

## Materials and Methods

### 4D image reconstruction using ART

Image reconstruction of 4D spectral-spatial imaging was based on ART [15, 35]. We extended the algorithm of 3D ART [35] to the computation dealing with 4D image data. The flowchart of the ART process is given in Fig. 1a. When each voxel has an EPR spectrum with $m$ data points in the magnetic field domain, the 4D image $\boldsymbol{s}_{4D}$ consists of EPR spectral data at each voxel and is written as a column vector ($mn \times 1$):

$$\boldsymbol{s}_{4D} = (\boldsymbol{s}_1^{T}, \cdots, \boldsymbol{s}_n^{T})^{T}, \quad (1)$$

where a column vector $\boldsymbol{s}_i$ ($m \times 1$) represents the EPR spectrum with $m$ elements (data points) at the $i$-th voxel. The transpose of the column vector is indicated by T. From the 4D image $\boldsymbol{s}_{4D}$, the spectral projection $\boldsymbol{f}_j$ [a column vector ($m \times 1$)] under magnetic field gradient $\boldsymbol{G}_j$, where $j$ represents the index of the magnetic field gradients, is given by

$$\boldsymbol{f}_j = \boldsymbol{A}_j \boldsymbol{s}_{4D}, \quad (2)$$

where $\boldsymbol{A}_j$ is the operator producing the spectral projection under magnetic field gradient $\boldsymbol{G}_j$ and is an ($m \times mn$) matrix. After calculating the spectral projection $\boldsymbol{f}_j$, the difference $\Delta\boldsymbol{f}_j$ between the measured spectral projection $\boldsymbol{f}_j^{\mathrm{meas}}$ and the computed spectral projection $\boldsymbol{f}_j$ is given by

$$\Delta\boldsymbol{f}_j = \boldsymbol{f}_j^{\mathrm{meas}} - \boldsymbol{f}_j . \quad (3)$$

Next, we updated the 4D image as

$$\boldsymbol{s}_{4\mathrm{D},j+1} = \boldsymbol{s}_{4\mathrm{D},j} + \boldsymbol{A}_j^{\mathrm{T}} \boldsymbol{w}_j^{-1} \Delta\boldsymbol{f}_j , \quad (4)$$

where $\boldsymbol{s}_{4\mathrm{D},j+1}$ and $\boldsymbol{s}_{4\mathrm{D},j}$ mean the updated and previous images, and $\boldsymbol{w}_j$ denotes the ($m \times m$) matrix of weight coefficients at diagonal elements:

$$\boldsymbol{w}_j = \mathrm{diag}\left(w_{j,1}, \cdots, w_{j,m}\right) . \quad (5)$$

Weight coefficient $w_j$ represents how many times each point in $\Delta\boldsymbol{f}_j$ will be placed on the image by the back projection operator $\boldsymbol{A}_j^{\mathrm{T}}$. Once this process [Eq. (2) to Eq. (4)] is completed for a given spectral projection, the 4D image is repeatedly updated again for each spectral projection under the magnetic field gradient ($j$ =1 to $k$, where $k$ is the total number of spectral projections). The 4D image is then updated with the spectral projections ($j$ =1 to $k$), and this is repeated until the 4D image converges. This repetition is called the iteration of ART processing ($q$ in Fig. 1a). In Eq. (4), the updating term may be weighted by a given coefficient (<1) to reduce the variance of the resultant image; however, it leads to a slower convergence. After each iteration of ART processing, a Gaussian filter [standard deviation = 0.69 mm (isotopic voxel size)] in 3D space was applied to the 4D image. This suppresses unwanted spatial variance (noise or artifacts) of the spectra in 3D space.

The ART computation code was implemented in the Fortran 95 development environment (Absoft Pro Fortran 2022, Absoft Corp., Rochester Hills, MI, USA). Parallel computing was implemented with the OpenMP Application Program Interface 3.1. Image reconstruction was performed on an Apple Mac mini computer (Intel Core i7, memory 16

GB). A trick of accelerating the computation of Eq. (4) is given as a Suppl. Text S1 in ESM.

**Concept of spectral projection synthesis**

In spectral-spatial EPR imaging, spectral projections are recorded with a data acquisition sequence under a systematically changing magnetic field gradient from $+G_{max}$ to $-G_{max}$ in a one-dimensional (1D) case. For a 3D subject having spectral information at each position (4D image data), the spectral projection $f$ at the magnetic field $B$ under magnetic field gradient $\boldsymbol{G}$ is given by the integration of EPR spectra shifted in the magnetic field domain:

$$f(B) = \int_{\mathbb{R}^3} s(B + \boldsymbol{G} \cdot \boldsymbol{r}, \boldsymbol{r}) d\boldsymbol{r}. \quad (6)$$

Here, $s$ represents the EPR spectrum at the position $\boldsymbol{r}$. We do not assume any symmetry of a spectral lineshape.

The flowchart of processing for computational spectral synthesis is given in Fig. 1b. At the computational spectral synthesis stage, the spectral changes of each position are unknown. However, the spectral projection under the magnetic field gradient (Fig. 2a) can be approximately obtained by a convolution process of the zero-gradient spectrum $s_0$ (Figs. 2b and 2c for a 1D example) and a flipped apparent spatial distribution $\hat{t}_a$ of the signal (Fig. 2d). We imposed the spectral differences at each position onto the spatial distribution of EPR signals in fitting the spectral projection $f_G$ under a magnetic field gradient $\boldsymbol{G}$:

$$f_G(B) \approx \int_{-\infty}^{\infty} \hat{t}_a(\boldsymbol{G}, \beta) s_0(B + \beta)\, d\beta, \quad (7)$$

where $\beta$ is a parameter of the convolution integral. This apparent spatial distribution differs from the actual spatial distribution of the signals. To fit the measured spectral projection $f_G$ by Eq. (7) (Figs. 2e and 2f), the apparent spatial distribution of the signal was obtained by the following optimization problem:

$$\arg\min_{\hat{t}_a} \frac{1}{2}\|f^{meas} - f^{comp}\|_2^2 + \lambda\|\nabla\hat{t}_a\|_1, \quad (8)$$

where $f^{comp}$ is the computed spectral projection [$f_G$ in Eq. (7)], $\lambda$ is a coefficient of the regularization term, $\|\nabla\hat{t}_a\|_1$ denotes the total variation of the flipped apparent spatial distribution [36]. After we found the flipped apparent spatial distribution of the signal, we approximately obtained the spectral projection $f_{-G}$ under the reversed magnetic field gradient $-\boldsymbol{G}$ (Figs. 2g and 2h) using the apparent spatial signal distribution $t_a$:

$$f_{-G}(B) \approx \int_{-\infty}^{\infty} t_a(\boldsymbol{G}, \beta) s_0(B + \beta)\, d\beta. \quad (9)$$

Although this approach is not exact, it gave approximately a spectral projection under a reversed magnetic field gradient. In our approach, 4D image reconstruction is performed using ART, so at this stage of numerical synthesis of spectra, it is sufficient to obtain the spectral projection without knowing the spectral variations of each position.

The 1D profile $t_a$ can be obtained by the optimization problem with the known zero-gradient spectrum and the measured spectral projection at each magnetic field gradient [36]. This problem is essentially a deconvolution process; however, an approach using the optimization problem can overcome the drawbacks due to the division-by-zero problem and blurring with filtering in the deconvolution process in the Fourier domain. We obtained the 1D profile $t_a$ using a hill-climbing search, which is a simple optimization algorithm.

Based on this concept, image degradation can be prevented by synthesizing spectral projections even though the number of measured spectral projections is reduced. In the standard filtered back-projection (FBP) method, the directions of magnetic field gradients for recording spectral projections are in the range of polar coordinate angle $-\pi/2$ to $+\pi/2$. Spectral projections with the opposite magnetic field gradients are not usually recorded. However, each spectral projection is used to update the image sequentially in the ART. Therefore,

spectral projections overlapping with the spectra recorded in the opposite magnetic field gradients are also effective for reconstructing the image with ART.

In our previous reports on 4D spectral-spatial EPR imaging, 15-step magnetic field gradients were applied in the *x*-, *y*-, and *z*-directions (total projections $15^3 = 3375$) [15, 32–34]. In this article, we reduced the number of spectral projections in one direction ($15 \times 15 \times p$) as a proof-of-concept experiment ($15 \geq p \geq 8$) (see suppl. Fig. S1 in ESM). Regarding compressed sensing in MRI, *k*-space data can be directly acquired in random under-sampling as a subset of measurements, removing artifacts in image reconstruction [25]. We could also randomly obtain EPR spectral projections in the *x*-, *y*-, and *z*-directions as in MRI, in the future.

**Numerical phantom for testing image reconstruction**

To test our ART code, we first reconstructed the 4D image using a numerical phantom that mimicked three homogeneous solutions in tubes with different peak-to-peak EPR linewidths. The peak-to-peak Lorentzian linewidths were set to 33, 39, and 46 μT, roughly mimicking the linewidths of 1.0, 1.5, and 2.0 mM nitroxyl radical solutions (see the next section) under air-saturated conditions. To obtain the Voigt function (convolution of the Lorentzian function and Gaussian function), we set the full width at half maximum (FWHM) of the Gaussian function to 30 μT. The image matrix was 72 × 72 × 72 × 512 (three spatial dimensions and one spectral dimension). The spectral window was 1.5 mT. The field-of-view (FOV) was 50 mm × 50 mm × 50 mm in 3D space. A field gradient setting with 15 steps was used for the numerical phantom simulation with a maximum field gradient of 30 mT/m for each direction. Under these conditions, we generated 3375 noise-free spectral projections under magnetic field gradients using Eq. (6). Another set of spectral projections with white noise was also generated, where the maximum noise amplitude was 5% of the EPR signal amplitude.

**Chemicals**

The nitroxyl radical 4-oxo-2,2,6,6-tetramethylpiperidine-$d_{16}$;1-$^{15}$N-1-oxyl ($^{15}$N-PDT) was purchased from CDN Isotopes (product no. M-2327, Quebec, Canada). The nitroxyl radical *trans*-3,4-dicarboxy-2,2,5,5-tetra($^{2}H_3$)methylpyrrolidin-(3,4-$^{2}H_2$)(1$^{15}$N)-1-oxyl ($^{2}$H,$^{15}$N-DCP) was synthesized as previously reported [16]. All chemicals used were of analytical grade.

**Sample solutions**

The nitroxyl radical $^{15}$N-PDT was dissolved in phosphate-buffered saline (PBS) and used in concentrations of 1.0, 1.5, and 2.0 mM. Sample tubes (5.8 mm in inner diameter and 50 mm long) were filled with air-saturated $^{15}$N-PDT solutions (0.5 mL each) and sealed with Parafilm. Three sample tubes were placed in the resonator with a sample holder made of cross-linked polystyrene.

**Animal preparation**

All animal experiments were performed in compliance with the "Law for The Care and Welfare of Animals in Japan" and approved by the Animal Experiment Committee of Hokkaido University (approval no. 20-0118). Six-week-old BALB/c-*nu*/*nu* male mice were purchased from Japan SLC (Hamamatsu, Japan) and housed at five mice per cage in a climate-controlled room with a 12-h light 12-h dark cycle and room temperature of 23 ºC. The mice could access standard mouse diet and water *ad libitum*. They were acclimated to their environment for a week before cell inoculation. The human-derived pancreatic ductal adenocarcinoma cell line Hs766T was purchased from the American Type Culture Collection (ATCC, Manassas, VA). Approximately 10 million Hs766T cells were subcutaneously inoculated into the right hind legs of mice. Tumors developed over 9–16 weeks until the

tumor volume reached 900 to 1000 $mm^3$. The mice were 16–23 weeks old and weighed 20–22 g at the time of EPR and MR image scanning.

**EPR spectrometer and imager**

A 750-MHz laboratory-built CW-EPR spectrometer/imager was used for EPR measurements. This spectrometer/imager has been reported previously [18]. In brief, a multi-coil parallel-gap resonator with a sample space of 22 mm diameter and 30 mm long was used in the reflection-type EPR bridge [37, 38]. The conversion efficiency of the RF magnetic field was 32 $\mu T/W^{1/2}$ at the center of the resonator. A permanent magnet system (static magnetic field 26.8 mT) was used with the coils of magnetic field gradients and the magnetic field scanning coil. The quality factor of the unloaded resonator was 420. Also, the quality factor with the $^{15}$N-PDT sample solutions was 330. For reference, when a tumor-bearing leg was inserted into the resonator, the quality factor was down to 100 or even lower [39].

**EPR imaging of the sample solutions**

Sample solutions with three different concentrations of $^{15}$N-PDT were placed in the resonator. The measurement parameters for EPR imaging were as follows: incident RF power 0.9 mW, magnetic field scanning 1.5 mT, field scan duration 100 ms, magnetic field modulation 0.04 mT at 90 kHz, time constant of lock-in amplifier 0.1 ms, number of data acquisition points per scan of 512, and maximum magnetic field gradient of 30 mT/m for each direction. The central magnetic field was set at a low field component of the EPR absorption peaks of $^{15}$N-PDT. The number of projections was set to $15^3$ (3375). The total acquisition time was 7.5 min. EPR imaging of the sample solution was conducted at room temperature. The spin system was below saturation and in the linear response region.

**In vivo EPR imaging of the mouse xenograft models**

The Hs766T tumor xenograft model was measured to perform Lorentzian linewidth mapping. For spectral-spatial EPR imaging, a tumor-bearing mouse was anesthetized by inhalation of isoflurane (1.3–2.0%). The subject mouse was placed prone on a mouse-holder made of cross-linked polystyrene. The right tumor-bearing leg of the subject mouse was placed in the RF resonator. Mouse body temperature and respiration were monitored with a fiber optic temperature sensor and a small air-pressure sensor. Mouse body temperature was maintained at 37.0 ± 0.5 °C by heated airflow regulated by a small-animal monitoring system (Model 1025, SA Instruments, Inc., Stony Brook, NY, USA). $^{2}$H,$^{15}$N-DCP was dissolved in 5 mM PBS (salinity 69 mM), and the solution was adjusted to pH 7.4 by adding NaOH or HCl. The mouse tail vein was cannulated for the intravenous injection of $^{2}$H,$^{15}$N-DCP. The infusion of $^{2}$H,$^{15}$N-DCP (0.4 mmol/kg body weight) was conducted over 40 s. $^{2}$H,$^{15}$N-DCP has narrower EPR absorption peaks and a longer lifetime of EPR signals than $^{15}$N-PDT in subject mice. The EPR signal acquisition was started 1 min after the infusion of $^{2}$H,$^{15}$N-DCP was completed. The measurement parameters of *in vivo* EPR imaging were as follows: incident RF power 18.2 mW, magnetic field scanning 1.5 mT, field scan duration 100 ms, magnetic field modulation 0.04 mT at 50 kHz, time constant of lock-in amplifier 0.1 ms, number of data acquisition points per scan 512, and maximum magnetic field gradient of 30 mT/m. The total acquisition time was 7.5 min for 3375 projections. The number of spectral projections was retrospectively reduced to investigate the influence of the number of spectral projections on the resulting quality in linewidth mapping. In 4D ART processing, the FWHM of the Gaussian function was set to 39.2 μT to compute the Voigt function for $^{2}$H,$^{15}$N-DCP.

**Results**

**Image reconstruction test with a numerical phantom**

To test our computation code for 4D spectral-spatial image reconstruction, we performed 3D linewidth mapping with the spectral projections generated from the numerical phantom (Maximum noise amplitude was set to 5% of the EPR signal amplitude). We could reconstruct the linewidths in the numerical phantom in 3D space. A schematic illustration of the numerical phantom is shown in Fig. 3a, and the three pillars have different Lorentzian linewidths. First, the convergence profile of linewidths in each pillar is given in Fig. 3b. After 30 iterations of ART processing, the mean linewidths converged for the three pillars and ART processing was terminated. The plots and error bars of the convergence profiles show the mean and standard deviation (SD) of the linewidth data for each pillar. The reconstructed linewidths were 33.24 ± 0.58 μT for pillar #1, 39.17 ± 0.55 μT for pillar #2, and 45.98 ± 0.54 μT for pillar #3 (mean ± SD) at the 30th iteration. The relative standard uncertainty (SD/| mean |), a measure of uncertainty in linewidth mapping, showed the lowest value at pillar #3 (0.54 μT/45.98 μT = 0.012). The computation time of a single cycle of ART processing with 3375 spectral projections was 17 min. The reconstructed spectra at the center of each pillar and residuals are shown in Fig. 3c. Furthermore, volume rendering of the linewidth map is provided in Fig. 3d. The corresponding histogram of the linewidths for each pillar is shown in Fig. 3e. To evaluate the reconstructed image quality, we obtained the normalized root-mean-square error (NRMSE) of the linewidths in the reconstructed image with various numbers of spectral projections [3375 (15 × 15 × 15), 2475 (15 × 15 × 11), and 1800 projections (15 × 15 × 8)], as shown in Fig. 3f. We used the linewidths in the numerical phantom as the ground truth. While this NRMSE profile reflects the degradation of linewidth mapping, no remarkable difference in NRMSE was shown at the 30th iteration of ART. All NRMSE data with 5% white noise is listed in Suppl. Table S2 (see ESM).

**Experimental verification of the partial acquisition strategy with a sample solution**

To further test 4D spectral-spatial image reconstruction and to demonstrate the partial acquisition strategy with computational spectral synthesis, we measured $^{15}$N-PDT sample solutions (Fig. 4a). A volume-rendered image of the double-integrated EPR signal intensities depicts the geometry of the sample solution in Fig. 4b. The convergence profile of the linewidths in 4D spectral-spatial data is given in Fig. 4c for a complete set of spectral projections. In Fig. 4d, we compared the reconstructed spectra with the complete set (3375) of spectral projections and a subset (1800) of spectral projections with computational spectral synthesis. Figure 4e shows the NRMSE for the 3D linewidth maps for the three cases of spectral projections. The linewidth map at the 30th iteration of the ART processing was used as the reference map of NRMSE. Figure 4f shows the slice-selective map of the linewidths for the three tubes at the center of the sample solution in three cases: (i) the complete set of spectral projections (3375); (ii) the subset of spectral projections (1800); and (iii) the subset of spectral projections (1800) with computational spectral synthesis. All images were obtained at the 30th iteration of the ART processing. Furthermore, Fig. 4g shows the linewidth histograms for each tube. In Fig. 4g, the relative standard uncertainties of linewidths for three solutions were (i) 0.039, 0.022, and 0.017 for 3375 projections, (ii) 0.081, 0.055, and 0.102 for 1800 projections, and (iii) 0.088, 0.091, and 0.027 for 1800 projections with computational spectral synthesis. In the NRMSE computation, the linewidth map with a complete set of spectral projections was considered to be a reference map. This imaging of the sample solutions confirmed the recovery of the linewidth mapping quality with computational spectral synthesis. As a result, we demonstrated the feasibility of the partially acquiring strategy for spectral projections and computational spectral synthesis.

**In vivo linewidth mapping in a mouse xenograft model**

To demonstrate our strategy in 4D spectral-spatial imaging with mouse xenograft models, we scanned a mouse Hs766T tumor-bearing leg by EPR imaging. A volume-rendered image of linewidths of $^{2}H,^{15}N$-DCP in the tumor-bearing leg is depicted in Fig. 5a. Scattered red voxels (broader linewidths) appeared around the tumor-bearing leg because remarkable errors in linewidth estimation are induced at voxels with low signal intensities. A double-integrated EPR signal intensity map, reflecting the radical concentration, is given in Fig. 5b. The linewidth map is shown in Fig. 5c. Both maps were selected at the sagittal plane shown in Fig. 5a. The histogram of the 3D linewidth map is provided in Fig. 5d. Furthermore, we retrospectively reduced the number of spectral projections and computationally synthesized the spectral data before ART processing. Figures 5e and 5f show the linewidth maps with various numbers of spectral projections with and without spectral synthesis. Representative reconstructed EPR spectra are shown in Fig. 5g to compare them at voxels A and B indicated in Figs. 5c, 5e, and 5f. After spectral fitting using the Voigt function, the Lorentzian linewidths were obtained at voxel A: 25.0 μT for 3375 spectral projections, 28.9 μT for 1800 spectral projections, and 26.1 μT for 1800 spectral projections with spectral synthesis, and at voxel B: 28.9 μT for 3375 spectral projections, 33.0 μT for 1800 spectral projections, and 28.5 μT for 1800 spectral projections with spectral synthesis. The quantitative evaluation (NRMSE) of those maps is shown in Fig. 5h. We used the linewidth map with a complete set of spectral projections (Fig. 5c) as the reference for NRMSE computation. ART processing was terminated at the 10th iteration. When the subject mouse underwent EPR imaging, it was 23 weeks old. The mouse's body weight was 20.8 g, and the tumor volume reached 990 $mm^3$.

**Discussion**

For 4D spectral-spatial imaging with a numerical phantom, our results regarding the mean linewidths in each pillar agreed with the linewidth setting in the numerical phantom. The

relative standard uncertainty under the noise-free condition defines the lower limit of the scattering of the linewidths in image reconstruction. In the histogram, the three peaks of the linewidths were separated, as in a previous report [15]. These results indicate that our 4D image reconstruction code worked correctly. We concluded that our 4D reconstruction code could be used for spectral-spatial imaging experiments. The linewidths for the three pillars converged after the 20th iteration of the ART process (Fig. 3b). However, since the convergence profile could differ in another sample, one should pay attention to the convergence of the lineshapes in the 4D image data. We achieved the relative standard uncertainty of 0.012 in the numerical model with white noise; however, standard uncertainty can depend on the noise level of the experimental projection data.

We retrospectively applied our partial acquisition approach to the data measured using the sample solution. In Fig. 4e, the NRMSE value of the linewidth map for 1800 projections with computational spectral synthesis was lower than that with 1800 projections. In Fig. 4f, the shape of linewidth maps for the tubes with 1800 projections became larger than in other cases. This difference was due to the blurring of the image. In Fig. 4g, the relative standard uncertainties of linewidths for three solutions are comparable to the previous results of linewidth mapping for $^{2}H,^{15}N$-DCP solution [15]. For the linewidth histograms for the 2.0 mM sample solution in the middle and right panels in Fig. 4g, the relative standard uncertainties were 0.102 and 0.027, respectively. However, there is no significant difference when looking at both histograms. We further examined the data for the linewidths. The maximum and minimum values in the linewidth data for the 2.0 mM sample solution were 4.50 and 48.60 μT, respectively, for the data set of 1800 spectral projections and 40.70 and 47.40 μT, respectively, for the data set of 1800 spectral projections with spectral synthesis. Some outliers led to a larger standard uncertainty in the former linewidth data. However, those outliers were not depicted in the histogram in Fig. 4g (middle panel). This is the reason

for the significant difference in the relative standard uncertainties (for outliers, see Suppl. Fig. S2 in ESM). Our results suggest that computational synthesis of the spectral projections partly recovers the quality of the linewidth map degraded with fewer spectral projections. While the improvement in the error of the spatial map (Fig. 4f) was visible, the improvement in the linewidth histograms (Fig. 4g) was modest compared to the alteration in the spatial map in our experiments. However, this finding is encouraging for mapping the linewidths in mouse xenograft models. If there is redundancy of the information (intensity and spectral variations) in a sample for a specific direction, we could reduce the number of spectral projections in this direction with less impact on the resultant image. In our experiments, we reduced the measured spectral projections in the *x*-direction, which is the axis of the cylindrical sample space. From the complete set of spectral projections in the 3D raster MFG settings, several MFG settings from the foremost strong magnetic field gradient were removed in the sacrificed direction for comparison of the image quality.

We further demonstrated our 4D spectral-spatial mapping in mouse xenograft models. The Hs766T xenograft tumor model is known to be hypoxic [40]. The results of the linewidth map show narrow peak-to-peak linewidths in a tumor xenograft, close to the linewidth of $^{2}$H,$^{15}$N-DCP solution under the oxygen-free condition (20 μT at 1 mM $^{2}$H,$^{15}$N-DCP [15]). The linewidth map suggests that some of the Hs766T tumor is hypoxic and has a low agent concentration. This result is consistent with the previous report of tumor oxygen mapping in the Hs766T xenograft model [39]. The results of linewidth mapping with the xenograft model suggest that our 4D spectral-spatial imaging with the partial acquisition strategy can reflect the spectral lineshape of the imaging agent *in vivo*. Although the information redundancy in the mouse tumor-bearing leg is unknown *a priori*, the length of the tumor-bearing leg in the cylindrical axis of the resonator is usually longer than the tumor dimensions in perpendicular directions. Considering this, it might be appropriate to set the sacrificed direction to be the

cylindrical axis of the resonator (the *x*-direction). However, this is not always appropriate and depends on the sample.

Conceptually, ART can be applied to arbitrary incomplete sets of projections. However, in general, many projections give a better-reconstructed image quality than fewer projections. While a spectral projection in the direction opposite the magnetic field gradient has similar spatial information (but flipped) as formalized, it still contributes to the quality of image reconstruction. Since we update the 4D image data spectral projection-by-spectral projection, additional spectral projections should have the same effects as iteration on the ART process, updating and converging the 4D image data. Increasing the spectral projections improved the reconstructed 4D image, partly recovering its quality. This improvement in the 4D image quality is due to additional constraints that have a role in strengthening the data fidelity of the image.

Our approach has several limitations. First, to enable the computational synthesis of spectral projections, the magnetic field gradients must be linear and there must be no hysteresis in the intensity of magnetic field gradients. Moreover, filter characteristics and delays in magnetic field scanning should not damage the measured spectral projections. The performances of these EPR spectrometer/imager instruments are essential in our approach. Moreover, this article focused on reducing the spectral projections in one direction. However, another approach, such as random selection in the MFG settings, to reduce spectral projections could be considered further. Also, an approach to identify which projections can be skipped without compromising the image quality would be helpful for the future practice of the proposed concept. However, since the object image is unknown a priori, it is difficult to identify “skipped projections” before conducting image acquisition at the present development stage. Thus, this issue should be further investigated.

Based on the mathematical modeling given in Eqs. (2)–(4), we could computationally synthesize the spectral projections from the measured projections. Even if the incorrect adjustment of the RF phase affects the EPR lineshape, our approach could take such an error into account. The additional spectral projections help recover the image quality even when some measured spectral projections are removed, as demonstrated in the results. Also, the proposed approach of reducing the measured spectral projections accelerates data acquisition in spectral-spatial EPR imaging. Since small animal experiments always require fast 4D image acquisition, approaches that reduce the measured spectral projection are helpful.

Moreover, 4D spectral-spatial image reconstruction is time-consuming in general. ART processing for 30 iterations requires 12.5 h. Other approaches, like parallel computing and improved algorithms, could shorten this computation time. Furthermore, the scattering of the linewidths in 4D image reconstruction should be improved to obtain a more precise 3D linewidth map. To convert a linewidth map to a $pO_2$ map, we must consider the influence of the imaging agent concentration, which also affects the EPR linewidth [41]. However, this problem is beyond the scope of this article.

## Conclusion

An approach for reducing spectral projections combined with a computational spectral synthesis was demonstrated for a sample solution and a mouse tumor xenograft model. The results proved that an acceleration of 4D spectral-spatial imaging (46.7% reduction of the acquisition time) could be achieved with less degradation of image quality. This decrease in the time required for data acquisition in CW-EPR imaging partly solves the technical drawback in 4D spectral-spatial imaging in small animal experiments.

## Author contributions

MO and HH contributed to the study concepts and design. MO and MT contributed to developing the 4D ART code. MO, MT, and YK contributed to the data generation and analysis. KY, HY, and OI contributed to animal preparation. IAK contributed to synthesizing $^{2}H,^{15}N$-DCP nitroxyl radical agent. SM helped animal experiments. MO and HH contributed to manuscript preparation. All authors read and approved the final manuscript.

**Funding**

This work was supported by the Japan Society for the Promotion of Science (JSPS) KAKENHI grants JP21K18165 and JP22H00200 (to HH); JP20H00443 and JP20KK0250 (to IO); JP22K18435 (to SM); and JP22H03740 (to HY).

**Data availability**

The data that support the findings of this study are openly available in The Open Science Framework at https://doi.org/10.17605/OSF.IO/34HKG.

**Declarations**

**Conflict of Interest:** The authors declare that there are no competing interests.

**References**


1. Michiels C, Tellier C, Feron O (2016) Cycling hypoxia: A key feature of the tumor microenvironment. Biochim Biophys Acta 1866:76–86
2. Corbet C, Feron O (2017) Tumour acidosis: from the passenger to the driver's seat. Nat Rev Cancer 17:577–593
3. Wouters A, Pauwels B, Lardon F, Vermorken JB (2007) Review: implications of in vitro research on the effect of radiotherapy and chemotherapy under hypoxic conditions. Oncologist 12:690–712
4. Colliez F, Gallez B, Jordan BF (2017) Assessing Tumor Oxygenation for Predicting Outcome in Radiation Oncology: A Review of Studies Correlating Tumor Hypoxic Status and Outcome in the Preclinical and Clinical Settings. Front Oncol 7:10
5. Naz S, Kishimoto S, Mitchell JB, Krishna MC (2019) Imaging Metabolic Processes to Predict Radiation Responses. Semin Radiat Oncol 29:81–89
6. Rich LJ, Seshadri M (2015) Photoacoustic imaging of vascular hemodynamics: validation with blood oxygenation level-dependent MR imaging. Radiology 275:110–118
7. Gertsenshteyn I, Epel B, Barth E, Leoni L, Markiewicz E, Tsai HM, Fan X, Giurcanu M, Bodero D, Zamora M, Sundramoorthy S, Kim H, Freifelder R, Bhuiyan M, Kucharski A, Karczmar G, Kao CM, Halpern H, Chen CT (2021) Improving tumor hypoxia location in $^{18}$F-misonidazole PET with dynamic contrast-enhanced MRI using quantitative electron paramagnetic resonance partial oxygen pressure images. Radiol Imaging Cancer 3:e200104
8. Elas M, Williams BB, Parasca A, Mailer C, Pelizzari CA, Lewis MA, River JN, Karczmar GS, Barth ED, Halpern HJ (2003) Quantitative tumor oxymetric images from 4D electron paramagnetic resonance imaging (EPRI): methodology and comparison with blood oxygen level-dependent (BOLD) MRI. Magn Reson Med 49:682–691

9. Liu KJ, Gast P, Moussavi M, Norby SW, Vahidi N, Walczak T, Wu M, Swartz HM (1993) Lithium phthalocyanine: a probe for electron paramagnetic resonance oximetry in viable biological systems. Proc Natl Acad Sci U S A 90:5438–5442
10. Epel B, Bowman MK, Mailer C, Halpern HJ (2014) Absolute oxygen R1e imaging in vivo with pulse electron paramagnetic resonance. Magn Reson Med 72:362–368
11. Kishimoto S, Matsumoto KI, Saito K, Enomoto A, Matsumoto S, Mitchell JB, Devasahayam N, Krishna MC (2018) Pulsed Electron Paramagnetic Resonance Imaging: Applications in the Studies of Tumor Physiology. Antioxid Redox Signal 28:1378–1393
12. Ahn KH, Halpern HJ (2007) Spatially uniform sampling in 4-D EPR spectral-spatial imaging. J Magn Reson 185:152–158
13. Kuppusamy P, Chzhan M, Samouilov A, Wang P, Zweier JL (1995) Mapping the spin-density and lineshape distribution of free radicals using 4D spectral-spatial EPR imaging. J Magn Reson Ser B 107:116–125
14. Elas M, Ahn KH, Parasca A, Barth ED, Lee D, Haney C, Halpern HJ (2006) Electron paramagnetic resonance oxygen images correlate spatially and quantitatively with Oxylite oxygen measurements. Clin Cancer Res 12:4209–4217
15. Komarov DA, Hirata H (2017) Fast backprojection-based reconstruction of spectral-spatial EPR images from projections with the constant sweep of a magnetic field. J Magn Reson 281:45–50
16. Gorodetsky AA, Kirilyuk IA, Khramtsov VV, Komarov DA (2016) Functional electron paramagnetic resonance imaging of ischemic rat heart: Monitoring of tissue oxygenation and pH. Magn Reson Med 76:350–358
17. Bobko AA, Eubank TD, Voorhees JL, Efimova OV, Kirilyuk IA, Petryakov S, Trofimiov DG, Marsh CB, Zweier JL, Grigor'ev IA, Samouilov A, Khramtsov VV (2012) In vivo monitoring of pH, redox status, and glutathione using L-band EPR for assessment of

therapeutic effectiveness in solid tumors. Magn Reson Med 67:1827–1836

18. Sato-Akaba H, Kuwahara Y, Fujii H, Hirata H (2009) Half-life mapping of nitroxyl radicals with three-dimensional electron paramagnetic resonance imaging at an interval of 3.6 seconds. Anal Chem 81:7501–7506
19. Komarov DA, Samouilov A, Hirata H, Zweier JL (2021) High fidelity triangular sweep of the magnetic field for millisecond scan EPR imaging. J Magn Reson 329:107024
20. Eaton SS, Shi Y, Woodcock L, Buchanan LA, McPeak J, Quine RW, Rinard GA, Epel B, Halpern HJ, Eaton GR (2017) Rapid-scan EPR imaging. J Magn Reson 280:140–148
21. Tseitlin M, Dhami A, Eaton SS, Eaton GR (2007) Comparison of maximum entropy and filtered back-projection methods to reconstruct rapid-scan EPR images. J Magn Reson 184:157–168.
22. Qiao Z, Redler G, Epel B, Qian Y, Halpern H (2015) 3D pulse EPR imaging from sparse-view projections via constrained, total variation minimization. J Magn Reson 258:49–57
23. Lustig M, Donoho D, Pauly JM (2007) Sparse MRI: The application of compressed sensing for rapid MR imaging. Magn Reson Med 58:1182–1195
24. Johnson DH, Ahmad R, He G, Samouilov A, Zweier JL (2014) Compressed sensing of spatial electron paramagnetic resonance imaging. Magn Reson Med 72:893–901
25. Feng L, Benkert T, Block KT, Sodickson DK, Otazo R, Chandarana H (2017) Compressed sensing for body MRI. J Magn Reson Imaging 45:966–987
26. Kimura K, Iguchi N, Nakano H, Yasui H, Matsumoto S, Inanami O, Hirata H (2022) Redox-sensitive mapping of a mouse tumor model using spares projection sampling of electron paramagnetic resonance. Antioxid Redox Signal 36:57–69
27. Zhang Z, Epel B, Chen B, Xia D, Sidky EY, Qiao Z, Halpern H, Pan X (2023) 4D-image reconstruction directly from limited-angular-range data in continuous-wave electron paramagnetic resonance imaging. J Magn Reson 350:107432

28. Zhang Z, Epel B, Chen B, Xia D, Sidky EY, Halpern H, Pan X (2024) Accurate reconstruction of 4D spectral-spatial images from sparse-view data in continuous-wave EPRI. J Magn Reson 361:107654
29. Ahn KH, Halpern HJ (2007) Simulation of 4D spectral-spatial EPR images. J Magn Reson 187:1–9
30. Ahn KH, Halpern HJ (2007) Comparison of local and global angular interpolation applied to spectral-spatial EPR image reconstruction. Med Phys 34:1047–1052
31. Ahmad R, Vikram DS, Clymer B, Potter LC, Deng Y, Srinivasan P, Zweier JL, Kuppusamy P (2007) Uniform distribution of projection data for improved reconstruction quality of 4D EPR imaging. J Magn Reson 187:277–287
32. Komarov DA, Ichikawa Y, Yamamoto K, Stewart NJ, Matsumoto S, Yasui H, Kirilyuk IA, Khramtsov VV, Inanami O, Hirata H (2018) In Vivo Extracellular pH Mapping of Tumors Using Electron Paramagnetic Resonance. Anal Chem 90:13938–13945
33. Taguchi A, DeVience S, Driesschaert B, Khramtsov VV, Hirata H (2020) *In vitro* simultaneous mapping of the partial pressure of oxygen, pH and inorganic phosphate using electron paramagnetic resonance. Analyst 145:3236–3244
34. Nakaoka R, Kato K, Yamamoto K, Yasui H, Matsumoto S, Kirilyuk IA, Khramtsov VV, Inanami O, Hirata H (2023) Electron Paramagnetic Resonance Implemented with Multiple Harmonic Detections Successfully Maps Extracellular pH In Vivo. Anal Chem 95:3940–3950
35. Komarov DA, Samouilov A, Ahmad R, Zweier JL (2020) Algebraic reconstruction of 3D spatial EPR images from high numbers of noisy projections: An improved image reconstruction technique for high resolution fast scan EPR imaging. J Magn Reson 319:106812
36. Yokoyama T, Taguchi A, Kubota H, Stewart NJ, Matsumoto S, Kirilyuk IA, Hirata H

(2019) Simultaneous $T_2^*$ mapping of $^{14}N$- and $^{15}N$-labeled dicarboxy-PROXYLs using CW-EPR-based single-point imaging. J Magn Reson 305:122–130

37. Kawada Y, Hirata H, Fujii H (2007) Use of multi-coil parallel-gap resonators for co-registration EPR/NMR imaging. J Magn Reson 184:29–38
38. Sato-Akaba H, Fujii H, Hirata H (2008) Improvement of temporal resolution for three-dimensional continuous-wave electron paramagnetic resonance imaging. Rev Sci Instrum 79:123701
39. Nakaoka R, Komarov DA, Matsumoto S, Hirata H (2018) Impact of the characteristic impedance of coaxial lines on the sensitivity of a 750-MHz electronically tunable EPR resonator. Appl Magn Reson 49:853–867
40. Wojtkowiak JW, Cornnell HC, Matsumoto S, Saito K, Takakusagi Y, Dutta P, Kim M, Zhang X, Leos R, Bailey KM, Martinez G, Lloyd MC, Weber C, Mitchell JB, Lynch RM, Baker AF, Gatenby RA, Rejniak KA, Hart C, Krishna MC, Gillies RJ (2015) Pyruvate sensitizes pancreatic tumors to hypoxia-activated prodrug TH-302. Cancer Metab 29:2
41. Halpern HJ, Peric M, Yu C, Bales BL (1993) Rapid quantitation of parameters from inhomogeneously broadened EPR spectra. J Magn Reson Ser A 103:13–22

**Figure Legends**

**Figure 1:** Flowcharts of processing for the algebraic reconstruction technique (ART) (**a**) and for synthesizing spectral projections (**b**). In flowchart **a**, parameter $k$ represents the total number of magnetic field gradients, $j$ indicates the index of the magnetic field gradients, and $q$ denotes the number of iterations for the ART process. In flowchart **b**, $\boldsymbol{G}$ represents the magnetic field gradient vector, $t_a$ represents an apparent spatial distribution of EPR signals, and $s_0$ means the zero-gradient spectrum. A "hat" notation means the flip of the spatial profile.

**Figure 2:** Concept of the partial acquisition of spectral projections and the computational synthesis of spectral projections. (**a**) Magnetic field gradients in the $z$-direction, (**b**) schematic cross-section of two sample tubes, (**c**) zero-gradient spectrum of $^{15}$N-PDT (the absorption peak at the lower field), (**d**) flipped apparent signal profile $\hat{t}_a$, (**e**) EPR spectral projections of $^{15}$N-PDT under a magnetic field gradient $G_z$ = +50 mT/m, (**f**) fitted spectral projection (red), (**g**) EPR spectral projections of $^{15}$N-PDT under a magnetic field gradient $G_z$ = –50 mT/m, and (**h**) computationally synthesized spectral projection (red).

**Figure 3:** Four-dimensional spectral-spatial imaging of a numerical phantom with ART. (**a**) A numerical phantom having different linewidths in 3D space, (**b**) convergence profile of peak-to-peak linewidths for three pillars, (**c**) reconstructed first-derivative EPR spectral lineshapes at the center of each pillar, and differences (reconstructed spectrum – given spectrum), (**d**) the volume-rendered image of peak-to-peak linewidths, (**e**) histograms of peak-to-peak linewidths for three pillars, and (**f**) normalized root-mean-square error (NRMSE) of the linewidth map with various reduction ratios of measured spectral projections. In panel **b**, the plots and error bars represent each pillar's mean and standard deviation (SD) of the

linewidth data. In panel **d**, the image matrix is 48 × 48 × 48, and the field-of-view (FOV) is 33.3 mm × 33.3 mm × 33.3 mm. The obtained linewidths are 33.24 ± 0.58 μT for pillar #1 (33 μT), 39.17 ± 0.55 μT for pillar #2 (39 μT), and 45.98 ± 0.54 μT for pillar #3 (46 μT) (mean ± SD). The values in parentheses are the linewidths given in the numerical phantom. The results in panels **c**, **d**, and **e** were obtained at the 30th iteration of ART processing.

**Figure 4:** 4D spectral-spatial imaging of a nitroxyl radical sample solution. (**a**) Photograph of glass tubes containing nitroxyl radical solutions (0.5 mL each, 5.8 mm in inner diameter and approximately 20 mm in length), (**b**) surface-rendered image of the EPR signal intensity, (**c**) convergence profile of the linewidths with 3375 spectral projections, (**d**) comparison of spectra reconstructed with all and a subset of spectral projections as well as computational spectral synthesis, (**e**) NRMSE of the linewidth maps with the three cases of spectral projections, (**f**) linewidth map of nitroxyl radicals (concentration 1.0 mM, 1.5 mM, and 2.0 mM), and (**g**) histograms of the linewidths for each solution. In panel **f**, the obtained linewidths with 3375 spectral projections are 33.66 ± 1.31 μT for a concentration of 1 mM, 40.74 ± 0.89 μT for a concentration of 1.5 mM, and 45.38 ± 0.76 μT for a concentration of 2.0 mM. [33.31 ± 2.69 μT, 40.35 ± 2.22 μT, and 44.42 ± 4.55 μT (1800 spectral projections); 32.45 ± 2.87 μT, 39.75 ± 3.63 μT, and 44.27 ± 1.20 μT (1800 spectral projections with spectral synthesis)]. The image matrix of the surface-rendered image in panel **b** is 48 × 48 × 48, and the FOV is 33.3 mm × 33.3 mm × 33.3 mm. This image was cut out from the image data of 72 × 72 × 72 and a FOV of 50 mm × 50 mm × 50 mm. The image matrix of slice-selective linewidth maps in panel **f** is 48 × 48, and the FOV is 33.3 mm × 33.3 mm. The results in panels **d**, **f**, and **g** were obtained at the 30th iteration of ART processing. The scale bar in panel **f** represents 5 mm.

**Figure 5:** EPR linewidth mapping in a mouse xenograft model. (**a**) Volume-rendered image of linewidths, (**b**) double-integrated EPR signal intensity map, (**c**) EPR linewidth map reconstructed from 3375 spectral projections, (**d**) histogram of the linewidths, (**e**, **f**) linewidth maps with and without the computational synthesis of spectral projections, (**g**) reconstructed EPR spectra at voxels A and B, and (**h**) NRMSE of the linewidth maps with and without spectral synthesis. In panel **a**, the image matrix of the volume-rendered image is 72 × 72 × 72, and the FOV is 50.0 mm × 50.0 mm × 50.0 mm. The image matrix of slice-selective EPR images is 48 × 48, and the FOV is 23.4 mm × 23.4 mm. The scale bar represents 5 mm. ART processing was terminated at the 10th iteration.

Figure 1

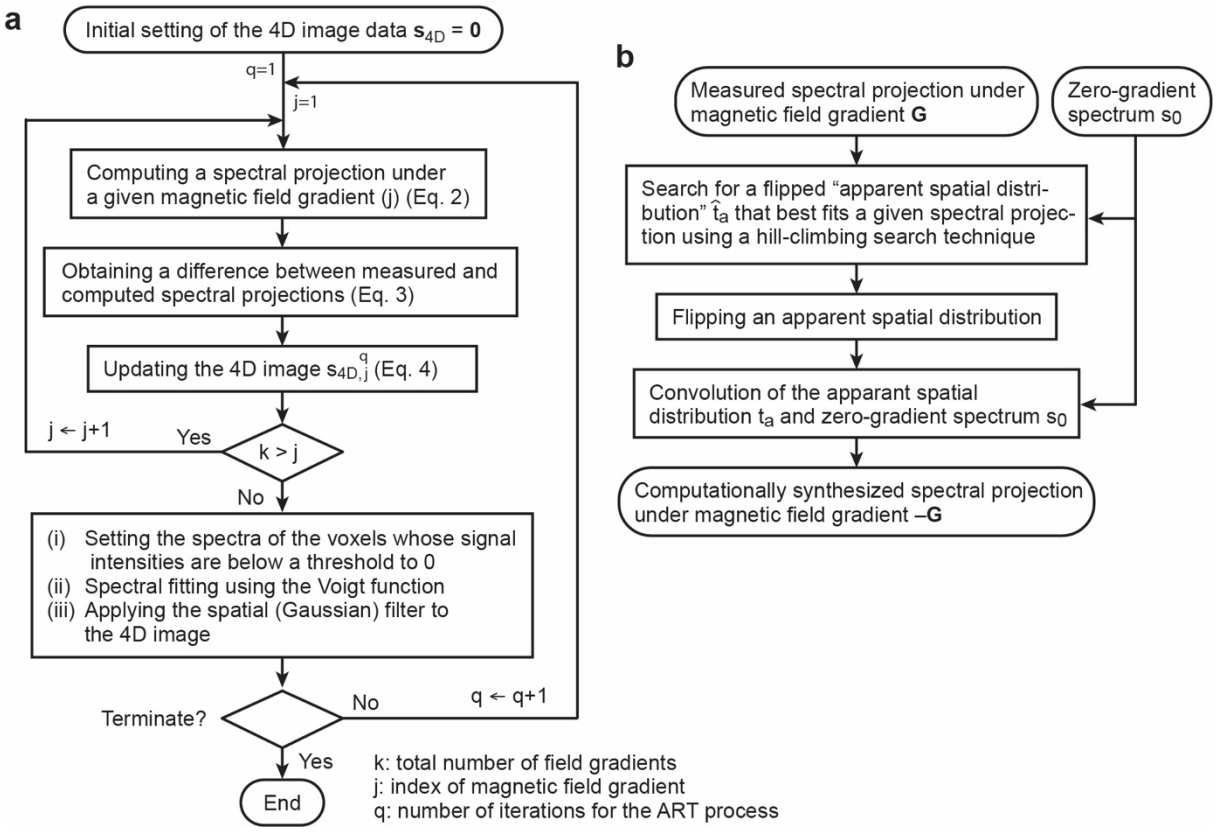


**Figure 1:** Flowcharts of processing for the algebraic reconstruction technique (ART) (**a**) and for synthesizing spectral projections (**b**). In flowchart **a**, parameter *k* represents the total number of magnetic field gradients, *j* indicates the index of the magnetic field gradients, and *q* denotes the number of iterations for the ART process. In flowchart **b**, ***G*** represents the magnetic field gradient vector, $t_a$ represents an apparent spatial distribution of EPR signals, and $s_0$ means the zero-gradient spectrum. A "hat" notation means the flip of the spatial profile.

Figure 2

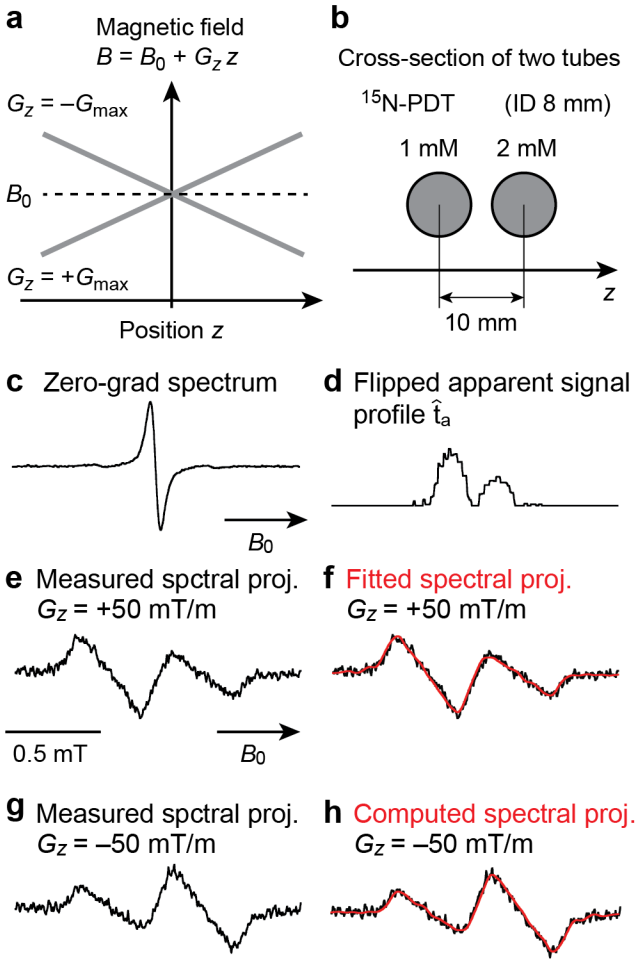


**Figure 2:** Concept of the partial acquisition of spectral projections and the computational synthesis of spectral projections. (a) Magnetic field gradients in the $z$-direction, (b) schematic cross-section of two sample tubes, (c) zero-gradient spectrum of $^{15}$N-PDT (the absorption peak at the lower field), (d) flipped apparent signal profile $\hat{t}_a$, (e) EPR spectral projections of $^{15}$N-PDT under a magnetic field gradient $G_z$ = +50 mT/m, (f) fitted spectral projection (red), (g) EPR spectral projections of $^{15}$N-PDT under a magnetic field gradient $G_z$ = –50 mT/m, and (h) computationally synthesized spectral projection (red).

Figure 3

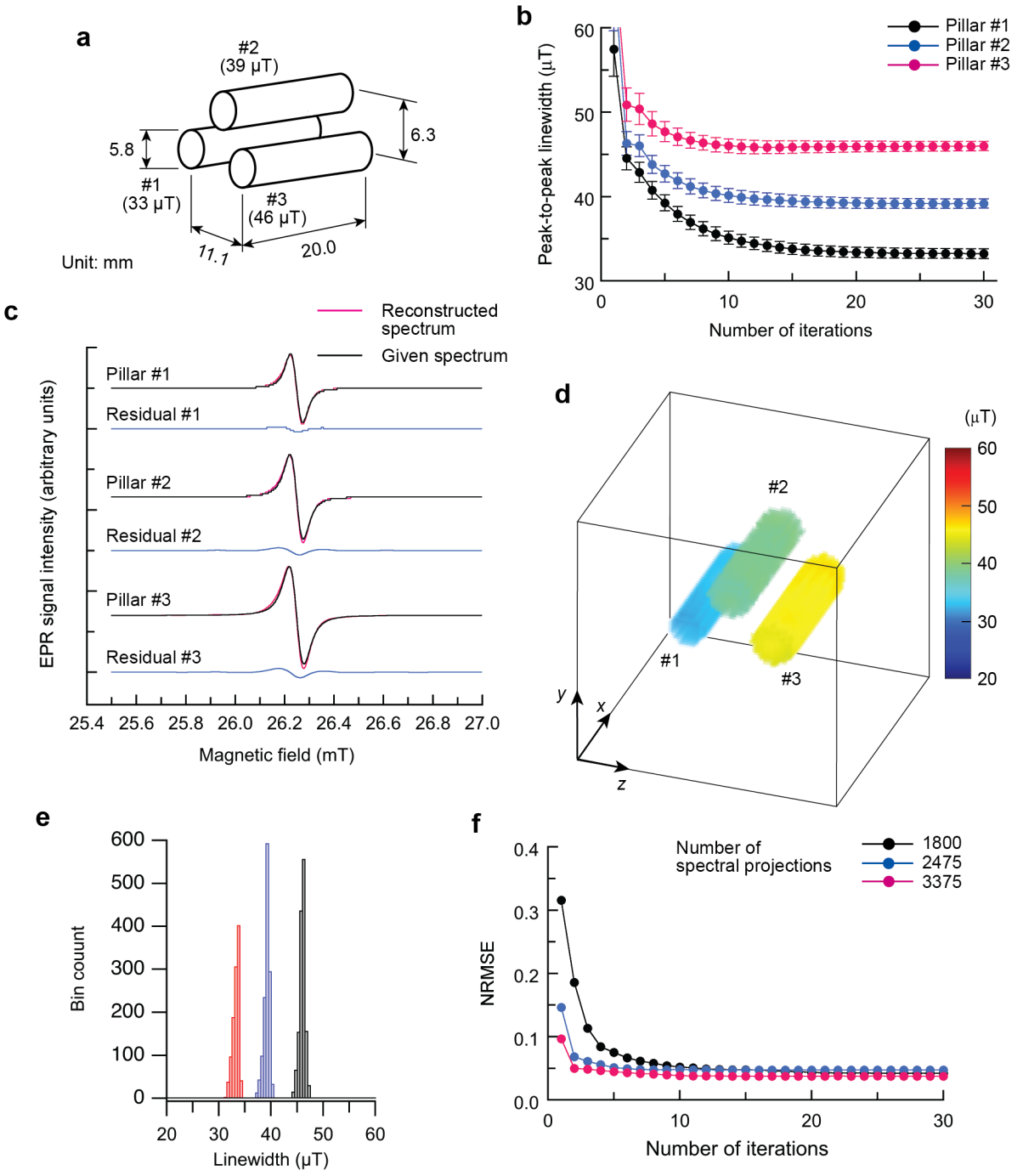


**Figure 3:** Four-dimensional spectral-spatial imaging of a numerical phantom with ART. (**a**) A numerical phantom having different linewidths in 3D space, (**b**) convergence profile of peak-to-peak linewidths for three pillars, (**c**) reconstructed first-derivative EPR spectral lineshapes at the center of each pillar, and differences (reconstructed spectrum – given spectrum), (**d**) the volume-rendered image of peak-to-peak linewidths, (**e**) histograms of peak-to-peak linewidths for three pillars, and (**f**) normalized root-mean-square error (NRMSE) of the linewidth map with various reduction ratios of measured spectral projections. In panel **b**, the plots and error bars represent each pillar's mean and standard deviation (SD) of the linewidth data. In panel **d**, the image matrix is 48 × 48 × 48, and the field-of-view (FOV) is 33.3 mm × 33.3 mm × 33.3 mm. The obtained linewidths are 33.24 ± 0.58 mT for pillar #1 (33 mT), 39.17 ± 0.55 mT for

pillar #2 (39 mT), and 45.98 ± 0.54 mT for pillar #3 (46 mT) (mean ± SD). The values in parentheses are the linewidths given in the numerical phantom. The results in panels **c**, **d**, and **e** were obtained at the 30th iteration of ART processing.

Figure 4

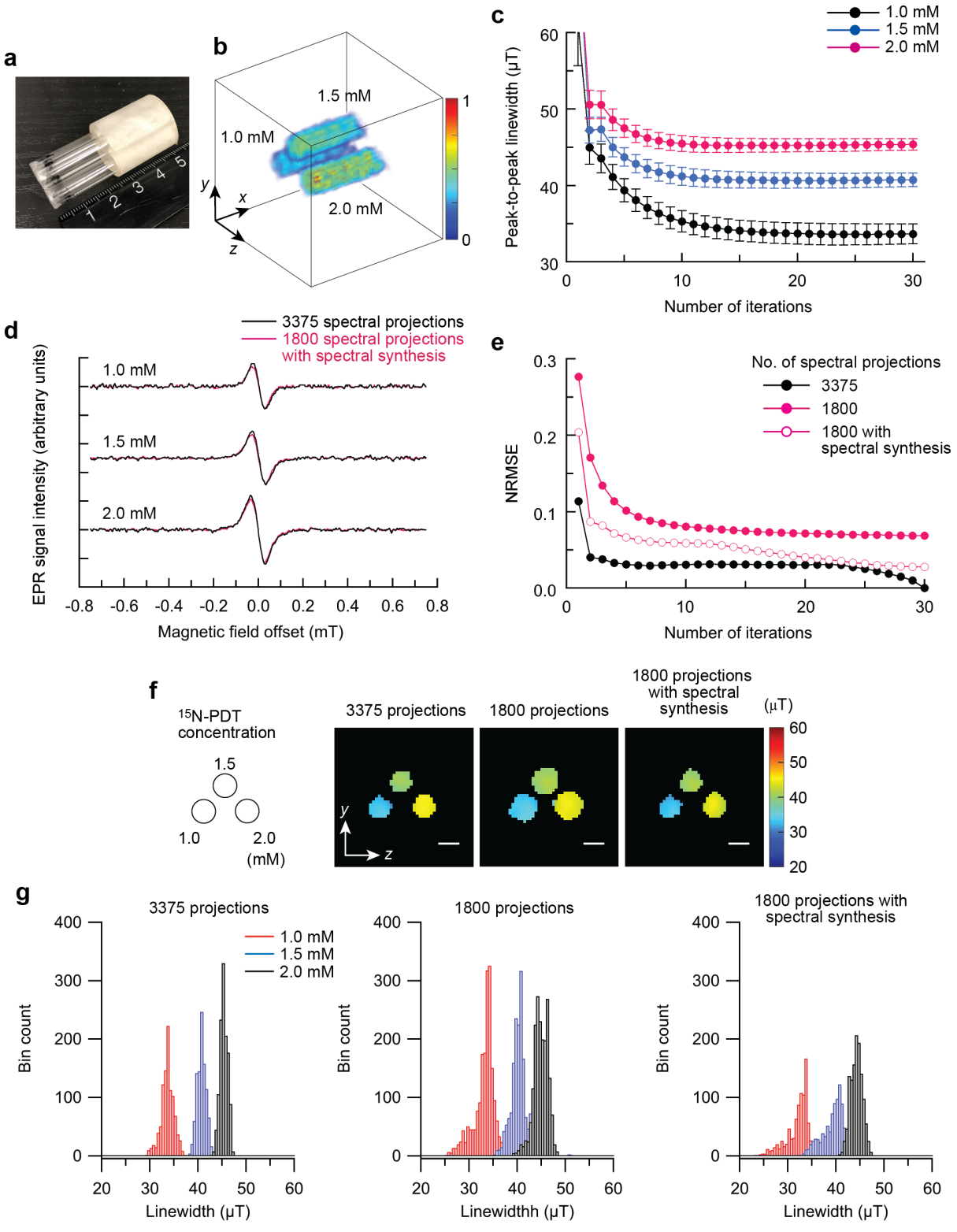


**Figure 4:** 4D spectral-spatial imaging of a nitroxyl radical sample solution. (**a**) Photograph of glass tubes containing nitroxyl radical solutions (0.5 mL each, 5.8 mm in inner diameter and approximately 20 mm in length), (**b**) surface-rendered image of the EPR signal intensity, (**c**) convergence profile of the linewidths with 1800 spectral projections with spectral synthesis, (**d**) comparison of spectra reconstructed with all and a subset of spectral projections as well as

computational spectral synthesis, (**e**) NRMSE of the linewidth maps with the three cases of spectral projections, (**f**) linewidth map of nitroxyl radicals (concentration 1.0 mM, 1.5 mM, and 2.0 mM), and (**g**) histograms of the linewidths for each solution. In panel **f**, the obtained linewidths with 3375 spectral projections are 33.66 ± 1.31 mT for a concentration of 1 mM, 40.74 ± 0.89 mT for a concentration of 1.5 mM, and 45.38 ± 0.76 mT for a concentration of 2.0 mM. [33.31 ± 2.69 mT, 40.35 ± 2.22 mT, and 44.42 ± 4.55 mT (1800 spectral projections); 32.45 ± 2.87 mT, 39.75 ± 3.63 mT, and 44.27 ± 1.20 mT (1800 spectral projections with spectral synthesis)]. The image matrix of the surface-rendered image in panel **b** is 48 × 48 × 48, and the FOV is 33.3 mm × 33.3 mm × 33.3 mm. This image was cut out from the image data of 72 × 72 × 72 and a FOV of 50 mm × 50 mm × 50 mm. The image matrix of slice-selective linewidth maps in panel **f** is 48 × 48, and the FOV is 33.3 mm × 33.3 mm. The results in panels **d**, **f**, and **g** were obtained at the 30th iteration of ART processing. The scale bar in panel **f** represents 5 mm.

Figure 5

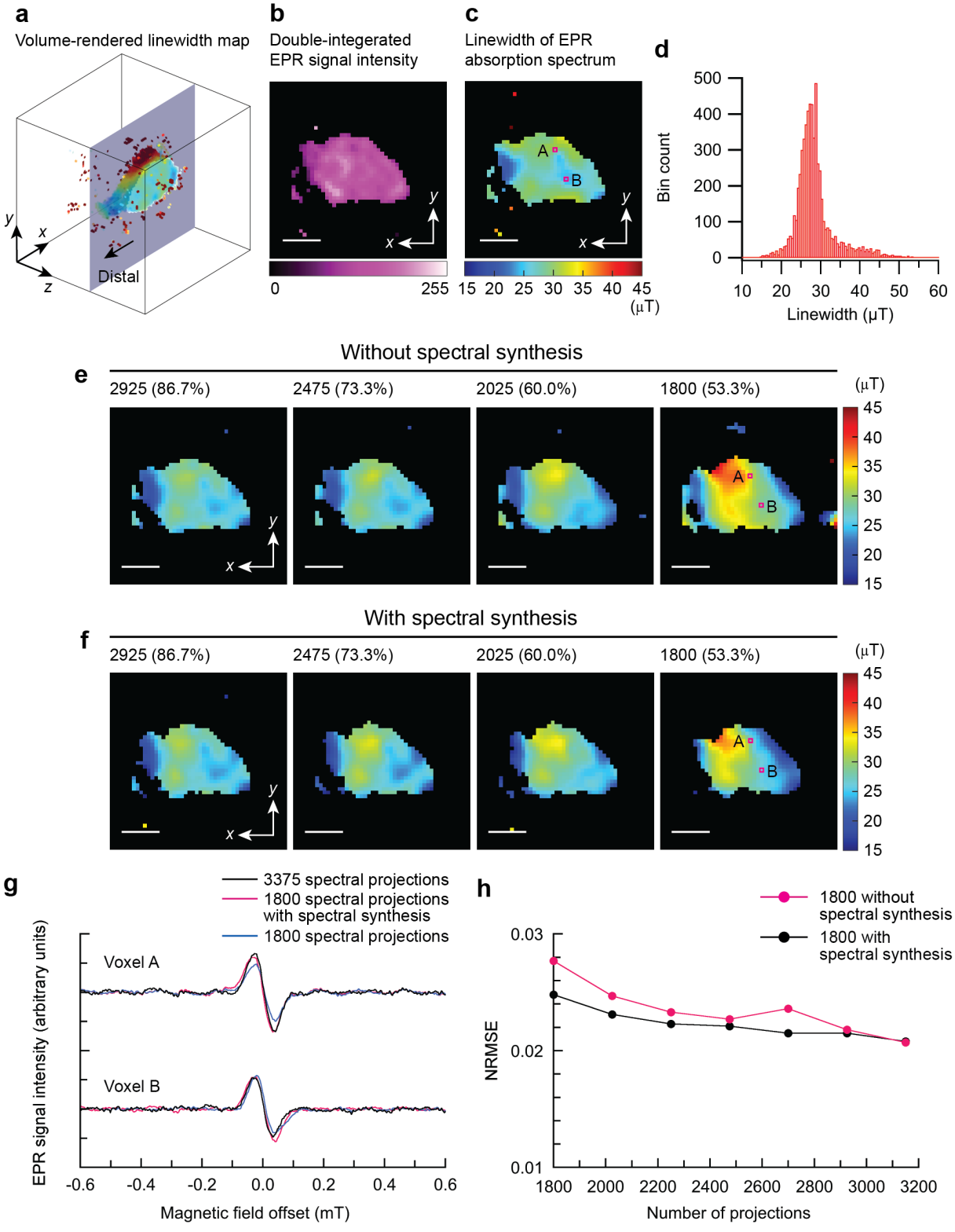


**Figure 5:** EPR linewidth mapping in a mouse xenograft model. (**a**) Volume-rendered image of linewidths, (**b**) double-integrated EPR signal intensity map, (**c**) EPR linewidth map reconstructed from 3375 spectral projections, (**d**) histogram of the linewidths, (**e**, **f**) linewidth maps with and without the computational synthesis of spectral projections, (**g**) reconstructed EPR spectra at voxels A and B, and (**h**) NRMSE of the linewidth maps with and without

spectral synthesis. In panel **a**, the image matrix of the volume-rendered image is 72 × 72 × 72, and the FOV is 50.0 mm × 50.0 mm × 50.0 mm. The image matrix of slice-selective EPR images is 48 × 48, and the FOV is 23.4 mm × 23.4 mm. The scale bar represents 5 mm. ART processing was terminated at the 10th iteration.